The Journal of Chemical Physics ARTICLE scitation.org/journal/jcp

Molecular simulations of sliding on SDS surfactant films

Cite as: J. Chem. Phys. 158, 244703 (2023); doi: 10.1063/5.0153397
Submitted: 7 April 2023 • Accepted: 5 June 2023 •
Published Online: 28 June 2023

Johannes L. Hörmann,[1,2,a)] Chenxu Liu (刘宸旭),[3] Yonggang Meng (孟永钢),[3] and Lars Pastewka[1,2]

AFFILIATIONS

[1]Department of Microsystems Engineering, University of Freiburg, Georges-Köhler-Allee 103, 79110 Freiburg, Germany
[2]Cluster of Excellence livMatS, Freiburg Center for Interactive Materials and Bioinspired Technologies, University of Freiburg, Georges-Köhler-Allee 105, 79110 Freiburg, Germany
[3]State Key Laboratory of Tribology in Advanced Equipment, Lee Shau Kee Science and Technology Building, Tsinghua University, Haidian District, Beijing 100084, China

Note: This paper is part of the JCP Special Topic on Adhesion and Friction.
[a)]**Author to whom correspondence should be addressed:** johannes.hoermann@imtek.uni-freiburg.de

ABSTRACT

We use molecular dynamics simulations to study the frictional response of monolayers of the anionic surfactant sodium dodecyl sulfate and hemicylindrical aggregates physisorbed on gold. Our simulations of a sliding spherical asperity reveal the following two friction regimes: at low loads, the films show Amonton's friction with a friction force that rises linearly with normal load, and at high loads, the friction force is independent of the load as long as no direct solid–solid contact occurs. The transition between these two regimes happens when a single molecular layer is confined in the gap between the sliding bodies. The friction force at high loads on a monolayer rises monotonically with film density and drops slightly with the transition to hemicylindrical aggregates. This monotonous increase of friction force is compatible with a traditional plowing model of sliding friction. At low loads, the friction coefficient reaches a minimum at the intermediate surface concentrations. We attribute this behavior to a competition between adhesive forces, repulsion of the compressed film, and the onset of plowing.

INTRODUCTION

In aqueous solutions, amphiphilic surfactants adsorb on immersed surfaces. Depending on the specific molecule and concentration, they form surface structures of varying morphologies: monolayers of flat-lying molecules, hemicylindrical stripes, or full cylinders have all been observed. The anionic model surfactant sodium dodecyl sulfate [SDS, see Fig. 1(a)] provides both molecular simplicity and a rich adsorption film phase diagram with transition from monolayers to hemicylinders.[1,2] Mechanical properties of SDS films depend on the adsorbate's concentration.[3,4] Even macroscopic frictional properties appear to be influenced by the concentration, and it has been hypothesized that this is related to the morphological transition in these films.[4] Since for ionic surfactants, adsorption and film morphology are controllable electrochemically, SDS adsorption films have become a model system for the study of electrotunable friction and lubrication.[4–11]

In this work, we use molecular calculations to probe SDS adsorption films at the Au(111)–water interface with a nanoscale sphere [see Fig. 1(b)], which can be representative of either a tip of an atomic force microscope (AFM) or an asperity on a rough surface. Specifically, we record the force–distance curves on the normal approach of a model AFM probe and friction-force measurements on the lateral sliding of the same probe on SDS adsorption films at the aqueous solution–Au(111) interface as conceptually shown in Fig. 2. We systematically explore the parametric space spanned by concentration, film morphology, and normal force. We find that single-asperity friction on these films has the following two distinct regions: at low loads, the friction force rises with the normal force before saturating, and both, the friction coefficient at low loads and the saturation force, depend on the film concentration.

SDS has been a model surfactant of colloidal science at least since the middle of the 20th century—a simple molecule with a complex phase diagram. Early experimental studies focused on

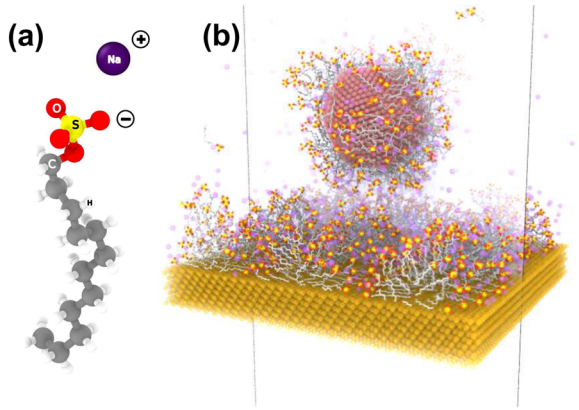

FIG. 1. (a) DS^- anion with hydrophilic sulfate head group and hydrophobic hydrocarbon tail and a Na^+ counterion comprise SDS. (b) Perspective view on the probe model sitting above hemicylindrical SDS aggregates.

properties of SDS micelles, which self-assemble at the critical micelle concentration (CMC) of about 8.2 mM.[12] At a high concentration of about 60 mM,[13–16] there is a transition to rod-like structures.[17–19] The number of molecules in the micelle, the aggregation number, appears to be around ~60 molecules and is independent of concentration for concentrations higher than the CMC but lower than the critical concentration for the transition to rods.[20] The whole phase diagram is more complicated, as micelles and rod can themselves self-assemble into crystalline or partially crystalline structures.

Micellization in bulk solution and the phase transition to hemicylindrical aggregates at interfaces arise due to the same hydrophobicity-induced self-organization mechanisms. SDS adsorption has been investigated for numerous idealized solid–solution systems, such as in the aqueous solution on graphite,[21–23] aluminum,[24] or gold.[1–3,25–27] Jaschke *et al.*[1] first showed direct atomic-force microscopy (AFM) images of stripe-like SDS-adsorption aggregates on the flat Au(111) and interpreted these as hemicylinders. They measured a spacing of 4.9 ± 0.5 nm between the stripes' central axes, and the same structures have also been observed on rough surfaces.[28] In the realm of electrochemistry, Burgess *et al.*[3] showed a potential-controlled transition from hemicylindrical to the condensed adsorption films for SDS on flat Au(111) (with an aggregate periodicity of 4.4 ± 0.5 nm). Their investigation was later extended onto a broad range of electrode potentials and SDS concentrations.[25] The parametric space spanned by electrode potential and surfactant concentration gives rise to at least four distinct adsorption film phases, namely complete desorption, flat monolayers, hemicylindrical aggregates, and possibly a compact bilayer phase.[2] SDS aggregation on other substrates, e.g.,

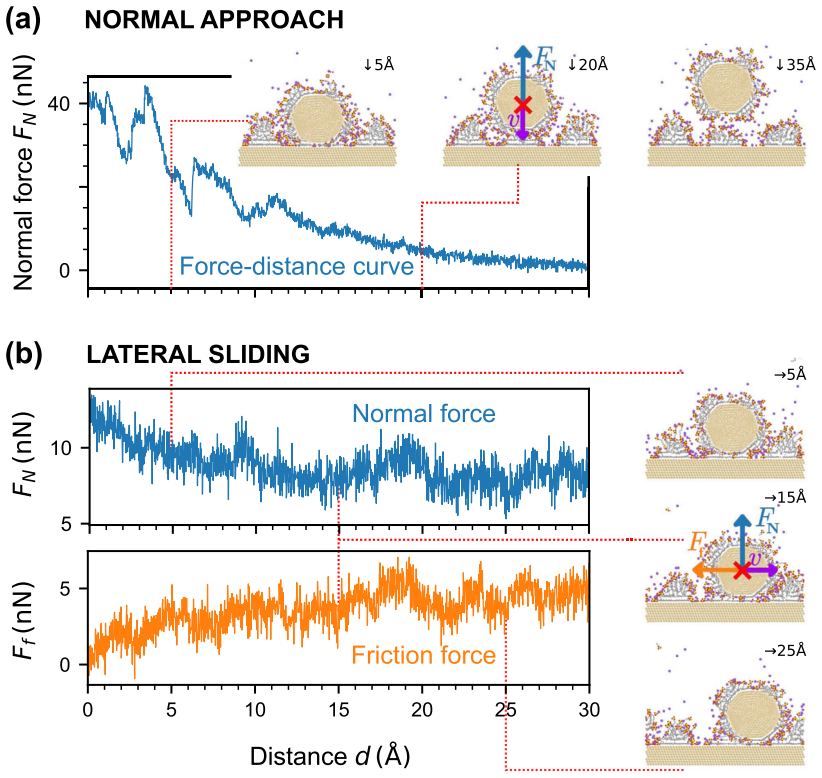

FIG. 2. (a) Normal approach force–distance curve at 1 m s^{-1} with snapshots at 35, 20, and 5 Å probe–substrate surface–surface distance. (b) Normal and friction force during lateral sliding at 1 m s^{-1} with snapshots at 5, 15, and 25 Å sliding distance and fixed probe–substrate distance of 9 Å.

on stainless steel,[29] graphite,[21,22] or oxidized graphene,[30] shows identical morphological transitions with concentration.

Film phase transitions may mean changing mechanical properties. Tribologists have investigated the boundary lubrication performance of SDS adsorption films, particularly, with a focus on the possibilities for electrotunable friction in macroscopic tribotests on stainless steel. Zhang and Meng[4,6] carried out sphere-on-disk experiments with a macroscopic zirconium dioxide probe of radius ~6 mm. They observed a change in the behavior across the transition from flat-lying monomers to hemicylindrical aggregates with increasing surfactant concentrations. In their series of experiments, the mean friction coefficient had a minimum at an intermediate SDS concentration, where surface aggregates consisted of densely packed monolayers. This appears to indicate a morphology-dependent change in the boundary lubrication behavior.

Zhang and Meng[6] argued that compared with dense films, stripe-like aggregates expose the metallic bulk between the stripes, leading to an increased likelihood of metal–metal junction formation. However, whether this observation is actually a consequence of morphology remains unclear. In particular, the direct contribution of film morphology at molecular scales as, e.g., probed in sliding experiments is not understood. Hence, we here model sliding experiments on SDS adsorption films at the H_2O–Au(111) interface by means of classical all-atom (AA) molecular dynamics (MD).

Important related systems studied by the friction community are organic friction modifiers (OFMs), a class of non-ionic surfactants, in oil. OFM adsorption films are referred to as self-assembled monolayers (SAMs).[31,32] Nonequilibrium simulations of OFMs[33,34] of such films are often studied in parallel-plate geometries, which have a constant film thickness and cannot describe plowing. More complex geometries, such as polymer-brush coated crossed cylinders[35,36] or OFM-covered AFM tips,[37] allow insights into the reorientation of the adsorbent molecules but require larger simulations. We here employ a sphere-on-flat geometry, since we believe that plowing the SDS film is a crucial friction mechanism.

METHODS

The prediction of adsorption isotherms for complex ionic molecules is presently out-of-reach for molecular calculations. To connect our molecular systems to experiments, we therefore experimentally characterize the adsorption of SDS molecules at the interface of an Au-coated quartz crystal sensor and SDS aqueous solution (0.01–20 mM) with a quartz crystal microbalance (QCM, Q-sense E4 system, Biolin Scientific, Sweden). The changes of both resonance frequency (Δf) and dissipation factor (ΔD) due to the mass variations of ions or molecules on the sensors per unit area are recorded by the QCM. We start the measurement in air to find the base resonance frequencies until approaching stable frequency values. Then, we inject pure water into the testing module by an external pump with the speed of 200 μl min^{-1} through polytetrafluoroethylene (PTFE) tubing, monitoring the fluctuations of ΔD and Δf in water until they stabilize. Finally, we switch the injection from pure water to the SDS solution and record the changes in ΔD and Δf caused by the adsorption or desorption of the ions or molecules for the third, fifth, seventh, and ninth overtones at 298 K. When the measured value of ΔD falls below 10^{-6}, we regard the adsorbed SDS as rigid and use the Sauerbrey equation $\Delta m = -C_0 \Delta f/N$ to calculate the adsorbed mass changes Δm from the frequency changes at the Nth overtone of the oscillations.[7,38,39] The *mass sensitivity constant* C_0 arises from the intrinsic material properties of the quartz crystal.[38] In this work, we use $C_0 = 17.7$ ng Hz^{-1} cm^{-2} for an AT-cut crystal with a fundamental resonance frequency $f_0 = 5$ MHz (Ref. 40, p. 201) and the third overtone for the calculation because of its better signal-to-noise ratio among the different overtones.

At selected configurations along this experimental adsorption isotherm, we carry out classical MD simulations employing a valence force field that allows the modeling of physisorption processes but does not include the breaking of covalent bonds. In the context of friction, we care about the explicit description of hydrogen atoms because coarse-grained models systematically underestimate frictional dissipation in non-equilibrium calculations.[41] Among all-atom parametrizations of SDS, the CHARMM branch has been established in a careful series of iterations[42–45] and used successfully for modeling micelles in bulk by several independent groups.[46–49] CHARMM36 can be combined with a parametrization for the interaction of molecules with solids including Au through the INTERFACE force field.[50] Hence, we use the CHARMM36 force field[51] and the rigid water model TIP3P (CHARMM standard,[45] non-zero hydrogen-hydrogen Lennard-Jones interaction parameters) as an explicit solvent. An embedded atom method potential by Grochola *et al.*[52] describes the Au–Au interactions. All other intermolecular interactions are modeled with CHARMM-standard force-switching Lennard-Jones interactions of 8 Å inner and 12 Å outer cutoff and force-shifting Coulomb interactions.[53–54] The latter are treated classically up to an 8 Å cutoff and with a particle-particle particle-mesh solver[55] beyond. All simulations run at standard conditions of temperature $T = 298$ K and pressure $P = 1013$ hPa. Except for initial thermalization, we use a Galilean-invariant dissipative particle dynamics (DPD) thermostat[56,57] applied only to the probe and the substrate (see below), but not the solvent and the salt.

All simulated systems consist of a model AFM probe of 5 nm diameter and substrate block of roughly $15 \times 15 \times 15$ nm^3 in size in a 3d-periodic box of about 32 nm total height. The probe and the substrate are composed of uncharged gold, with outer (111) planes facing each other. AFM probe models are prepared by melting gold spheres of 3873 atoms and a 2.5 nm initial radius and subsequent slow quenching from 1800 K down to 298 K over a time span of 100 ns using a 5 fs time step. This yields a single crystalline, almost spherical, gold probe shown in Fig. 1(b). The substrate is a cubic, single crystal gold block with one of its {111} surfaces exposed to the solution. All systems are solvated in water and carry zero net charges. SDS adsorption films cover the substrate and the probe. The specific size of the substrate was chosen to accommodate three hemicylindrical surfactant aggregates of ~2.5 nm radius.[1]

Sampling the full adsorption process from solution lies out of reach within the timescales accessible to brute-force MD.[58] Although free-energy calculations could, in principle, yield insights into the absorption process,[47] we here preassemble a set of monolayers and hemicylinders at appropriate surface concentrations to cover a wide range of the adsorption isotherm across the regime of film phase transition. Likewise, we assemble a uniform mono-

layer of equivalent surface concentrations around the probe to mimic the double-layer structure between the probe and the substrate. We arrange surfactant molecules on the surface of the minimal sphere enclosing the gold cluster and close the remaining gaps between the surfactant tail and flat facets by an artificial pulling force.

Both the preassembled probe and the substrate systems are solvated and relaxed in separate simulations. The relaxation procedure starts with an energy minimization, followed by 100 ps constant-temperature [particle number, volume, and temperature (NVT)] and 100 ps constant-pressure [particle number, pressure, and temperature (NPT)] equilibration under restrained ion positions. We regulate temperature by velocity rescaling with a stochastic term[59] at relaxation time 1 ps. A Berendsen barostat[60] controls pressure at relaxation time 4 ps. Those calculations are followed by an unrestrained 3 ns NPT relaxation of the preassembled adsorption layer. The probe and the substrate are merged at an initial distance of $d = 3$ nm—sufficiently far to not disturb the adsorption film structure. In the case of an overlap, the conflict is solved by removing the solvent molecules. If removing the solvent molecules alone cannot resolve the conflict (i.e., in the case of overlapping ions and substrate atoms), the ions in question are displaced randomly until the conflict can be resolved by removing solvent molecules only. The assembled system is then equilibrated according to the same sequence of NVT, NPT, and production condition relaxation runs. Here, the duration of each relaxation step is 20 ps. Temperature is controlled by a Langevin thermostat[61] of damping parameter 1 ps. A Nosé–Hoover barostat[62,63] with damping parameter 1 ps controls pressure. Eventually, we relax the system at production conditions for tempering only probe and substrate with the aforementioned DPD thermostat.[56,57]

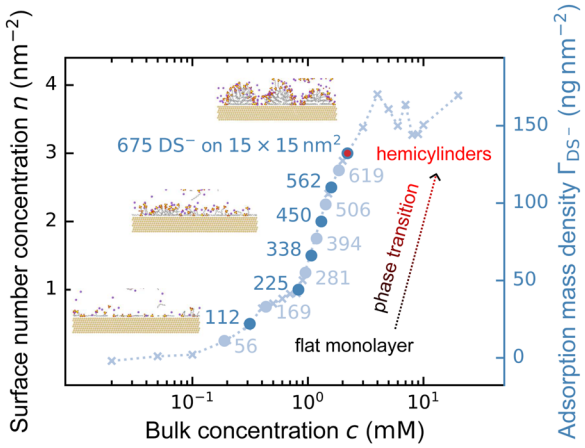

FIG. 3. Experimental adsorption isotherm of SDS on Au(111) in aqueous solution recorded by quartz crystal microbalance (QCM). Experimental measurements are indicated by "x" markers and connected by dotted lines. Solid circles mark concentrations for which molecular calculations are carried out. The values next to the solid circles give the actual numbers of DS$^-$ anions assembled on a 15 × 15 nm^2 gold substrate. Alternating light and dark coloring is intended as a guide to the eye.

For a normal approach, we set the probe's frozen core of 2.4 nm diameter into motion at a prescribed velocity of 0.1, 1, or 10 m s^{-1} as stated hereafter. The substrate's bottom-most 1.4 nm layer is also frozen to fix its position. For lateral sliding at fixed probe–substrate distances, we extract equidistant configurations along the normal approach trajectories. These individual snapshots are relaxed again for 20 ps without movement of the probe. We then assign a constant lateral velocity of 1 m s^{-1} to the probe's core. All surface–surface distances are stated with respect to the perfect overlap of the substrate's and probe's outermost atomic layer as zero reference.

Our sliding simulations are carried out at a constant height of the probe and at a fixed velocity of 1 m s^{-1}. In similar studies, friction forces and normal distances are often sampled under a constant normal force applied via a spring attached to the probe model.[37] Our approach avoids the introduction of an additional spring constant, suppressing the stick-slip motion[64] and the associated relaxation phenomena. From the perspective of macroscopic experiments on rough surfaces, our nanoscopic system may be understood as one single asperity in the contact on the timescale of nanoseconds. Each asperity is embedded in an elastic medium, which means that both normal distance and pressure change as the asperity makes and breaks contact during sliding. If the medium is stiff, it will not undergo considerable elastic deformation, and we approximate this

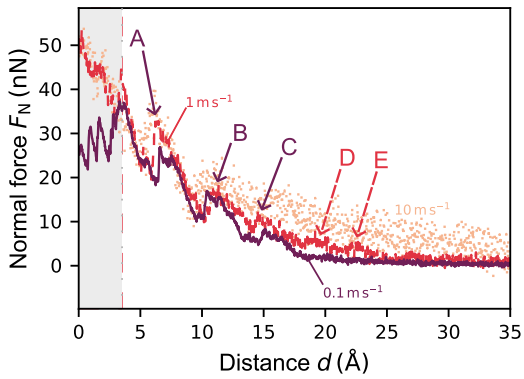

FIG. 4. Simulated AFM force–distance curves for a probe centered above hemicylindrical aggregate at velocities 10 m s^{-1} (light, dotted), 1 m s^{-1} (dashed), and 0.1 m s^{-1} (dark, solid). Data points are 0.2, 2, and 20 ps averages, respectively. Features A-C (dark purple arrows) are qualitatively observable in both 1 m s^{-1} and 0.1 m s^{-1} trajectories. Features D and E (dashed red arrows) are only observed in the 1 m s^{-1} trajectory.

TABLE I. Viscous drag in TIP3P water as estimated for a bead of $r = 2.5$ nm by Stokes' law and as recorded via MD for our AFM tip model in bulk solution.

Stokes drag of the AFM probe			
Velocity v (m s^{-1})	10	1	0.1
Analytical F_d (nN)	0.15	0.02	~0
MD, bare probe (Ref. 67) F_d (nN)	1.27	0.15	0.02
MD, covered probe F_d (nN)	1.41	0.38	0.18

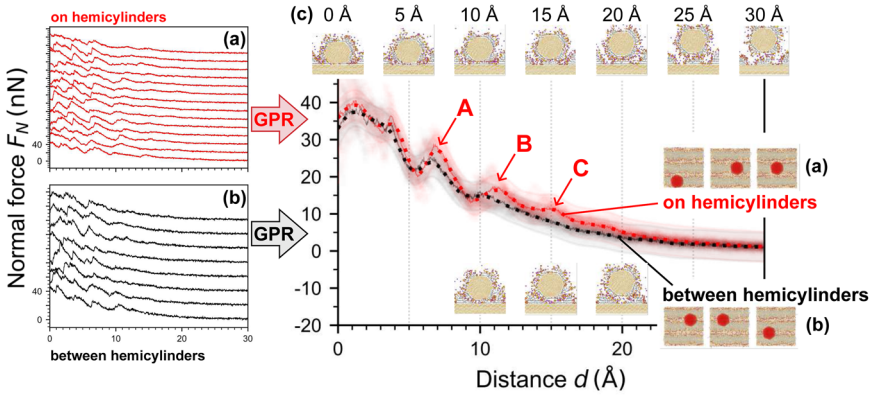

FIG. 5. (a) 12 AFM force–distance curves recorded at varying sites with the probe model centered above the hemicylinder apex (red), (b) 8 AFM force–distance curves recorded at varying sites with the probe model centered between two hemicylinders (black). Curves are offset by 20 nN. (c) Gaussian process regression on a set of trajectories of normal force–distance curves, each averaged over 2-ps intervals. Top-view insets labeled (a) and (b) show exemplary initial configurations for probing sites on and between hemicylinders. The model for probing sites at the hemicylinders' apex is colored red, whereas the model for sites exactly between the two hemicylinders is shown in black. A thin continuous line visualizes the simple mean of the 2 ps-averaged data points. Solid dots show the inferred Gaussian process means. The translucent bands mark the 95% confidence interval for the models. Underlying data points are indicated as transparent coloring with varying intensities. Upper snapshots display exemplary cross-sections of a probe approaching hemicylinders, and lower snapshots show a probe coming down between two hemicylinders. Red arrows point to features A–C present in the fit on trajectories with the probe centered above the hemicylinders.

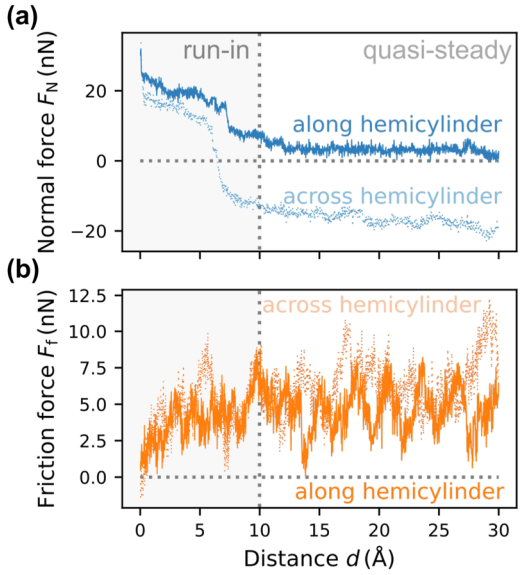

FIG. 6. Typical (a) sample normal force (blue) and (b) friction force (orange) signals for sliding across (dotted line) and along (solid line) a hemicylindrical adsorption aggregate at fixed a normal distance of 3 Å and 1 m s^{-1} velocity. In the case of sliding across the hemicylindrical aggregate, a gold–gold contact occurs beyond 5 Å lateral distance, resulting in an adhesive normal force.

process here by keeping the asperity at constant height. Our results are hence more representative of the contact of an individual asperity on a rough surface rather than an AFM tip that is typically connected to a soft cantilever.[65]

RESULTS

Figure 3 shows the experimentally recorded SDS adsorption isotherm on Au(111) in aqueous solution ranging from 0.25 nm^{-2} up to 3 nm^{-2} surface concentrations. Solid circles in Fig. 3 show the concentrations at which MD calculations are carried out. The labels next to these points give the corresponding number of molecules on a 15 × 15 nm^2 substrate. We cover the full concentration range from 0.1 mM up to saturation at about 3 mM, across which the adsorption film transitions from the flat-lying monolayers to hemicylindrical aggregates. At low-to-intermediate concentrations, samples are preassembled as monolayers. At high concentrations, we preassemble hemicylinders at the red discretization point at the upper concentration end, corresponding to 3 nm^{-2} or 675 molecules. These hemicylinders were stable over 50 ns, our longest molecular dynamics run. We consider this system representative of the plateau region that emerges at high bulk concentration. All our systems are homogeneous, i.e., either pure monolayers or hemicylinders, whereas in reality, mixed phases of monolayers and hemicylinders exist.[2,3]

Since we are interested in the effect of adsorption films on the force response, we first need to rule out that we are measuring the viscous drag of the solvent. Hence, we estimate the viscous drag of our model AFM probe in water at standard conditions by means of Stokes' law for a bead in viscous fluids, $F_d = 6\pi\eta r v$, with a probe radius of r = 2.5 nm using the reported dynamic viscosity of the TIP3P rigid water, η = 0.321 mPa s.[66] Additionally, we run probe normal approaches on the system illustrated in Fig. 1 for the velocities 10, and 0.1 m s^{-1} and show normal force vs distance in Fig. 4.

In our MD results, we interpret average forces acting on the probe at distances $5 \geq d > 4$ nm above the substrate as viscous drag. Table I summarizes the analytical and MD estimates. Both analytical estimate and MD results extracted from force–distance curves

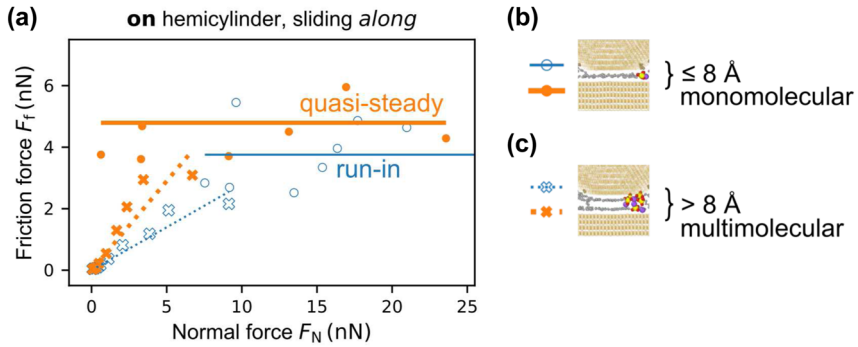

FIG. 7. (a) We label the initial 1 nm of sliding *run-in*, the subsequent sliding as *quasi-steady*, compute averages of friction and normal force for both sliding segments, and show these friction force–normal force pairs as blue (run-in) and orange (quasi-steady) data points here. (b) At normal distances of $z \leq 0.8$ nm, we speak of a monomolecular gap and show data points as circles. The mean friction force of these data points is shown by a solid horizontal line in (a). (c) At normal distances of $z > 0.8$ nm, we speak of a of multimolecular gap and show data points as crosses in (a). Linear fits with zero intercept to these data points are shown as dotted lines.

yield non-negligible drag for $v \gtrsim 10$ m s^{-1}. Viscous drag at speeds slower than 10 m s^{-1} is an order of magnitude lower than forces from resistance of the surfactant films. Deviations from analytical Stokes estimates up to an order of magnitude are likely due to hydrodynamic interactions between the tip and the surface at the distances of $\lesssim$5 nm probed here, which correspond just to a couple of hydration shells. The MD drag estimates for the film-covered probe approaching a hemicylindrical aggregate are larger than for the bare probe approaching a monolayer.[67]

In the force–distance curves of Fig. 4, there are at least three quantitatively relatable features marked by dark purple arrows A, B, and C at about 6, 11, and 15 Å. The latter two of these features are unidentifiable in the fast approach case of 10 m s^{-1}. Interestingly, the 1 m s^{-1} approach appears to exhibit two more features marked by red dashed arrows D and E at 19 and 22 Å that are not identifiable in the 0.1 m s^{-1} approach. Common to all MD results is the probe–substrate contact at about 4 Å distance and the onset of plastic deformation below, indicated by a gray area. Other than the two faster approaches, the 0.1 m s^{-1} approach velocity exhibits three subsequent deformation events and decreased repulsion below 3 Å normal distance.

All the following results use an approach velocity of 1 m s^{-1}, which is a compromise between reduced solvent drag and computational costs. Figures 5(a) and 5(b) show multiple approaches to hemicylinders. Each force–distance curve was recorded at different lateral offsets of the tip. More specifically, panel (a) shows the results for the approach of the probe on top of the hemicylinders, whereas panel (b) shows the results between hemicylinders. Top-down views of the selected configuration can be found in the insets of Fig. 5(c). Single normal approach curves in panels (a) and (b) clearly exhibit distinct features. As with the velocity-dependent force–distance curves of Fig. 4, it is difficult to identify a systematic dependence of the individual features on the site (on or between hemicylinders) of the approach.

We use stochastic variational Gaussian process regression,[68] a variant of Gaussian process regression (GPR)[69] suitable for large amounts of data, to fit trend lines to all force–distance curves in panels (a) and (b). Figure 5(c) shows the fit to the data shown in Figs. 5(a) and 5(b). Translucent bands indicate 95% confidence intervals. Insets at the top of Fig. 5(c) show 5 Å-spaced side views of one representative approach on top of hemicylinders along a cross-section as indicated in Fig. 1(b). Insets at the bottom show three such snapshots for an approach between the hemicylinders.

Although single trajectories such as those shown in Fig. 4 do not necessarily provide generalizable insights, the averages over many trajectories (obtained from GPR) in Fig. 5 filter out fluctuations and emphasize recurring features. The approach on the top of hemicylinders clearly shows several realignments or squeeze-out events absent from the approach between the hemicylinders. This is, in particular, the squeeze-out of multiple down to three molecular layers in the contact taking place around a normal distance of 15 Å (arrow C) and the transition from three to two molecular layers in the contact around 11 Å (arrow B).

The cross-sectional snapshots in Fig. 5 clearly show the absence of these transitions in the case of the probe coming down between two hemicylindrical aggregates. Below a normal distance of 10 Å, the force–distance curves do not show distinguishable features anymore. This corresponds to what is visible in the snapshots: In both cases, the contact is filled with two molecular layers at 10 Å, undergoes the squeeze-out to one molecular layer around 6–7 Å (arrow A), followed by the compression of the probe and the substrate around a few possibly trapped molecules or on direct gold–gold contact. Our GPR model shows that the features A–C in Fig. 4 are characteristic of the morphology, whereas features E and F appear to be random features of the specific realization of the film.

Such squeeze-out events are representative of AFM experiments on the surfactant films[3] or other confined liquids.[70] For well-prepared molecularly smooth convex surfaces, this oscillatory behavior due to liquid layering and thin-film structures is observable even in macroscopic surface force apparatus (SFA) experiments,[71] but naturally, this is not the case for rough surfaces.[72,73]

We now focus on the lateral sliding of these hemicylindrical aggregates. Sliding is carried out at constant height, and we separately show normal [Fig. 6(a)] and friction forces [Fig. 6(b)] as a function of the sliding distance d for a total distance of 3 nm. Preliminary runs for multiple periodic transitions across the peri-

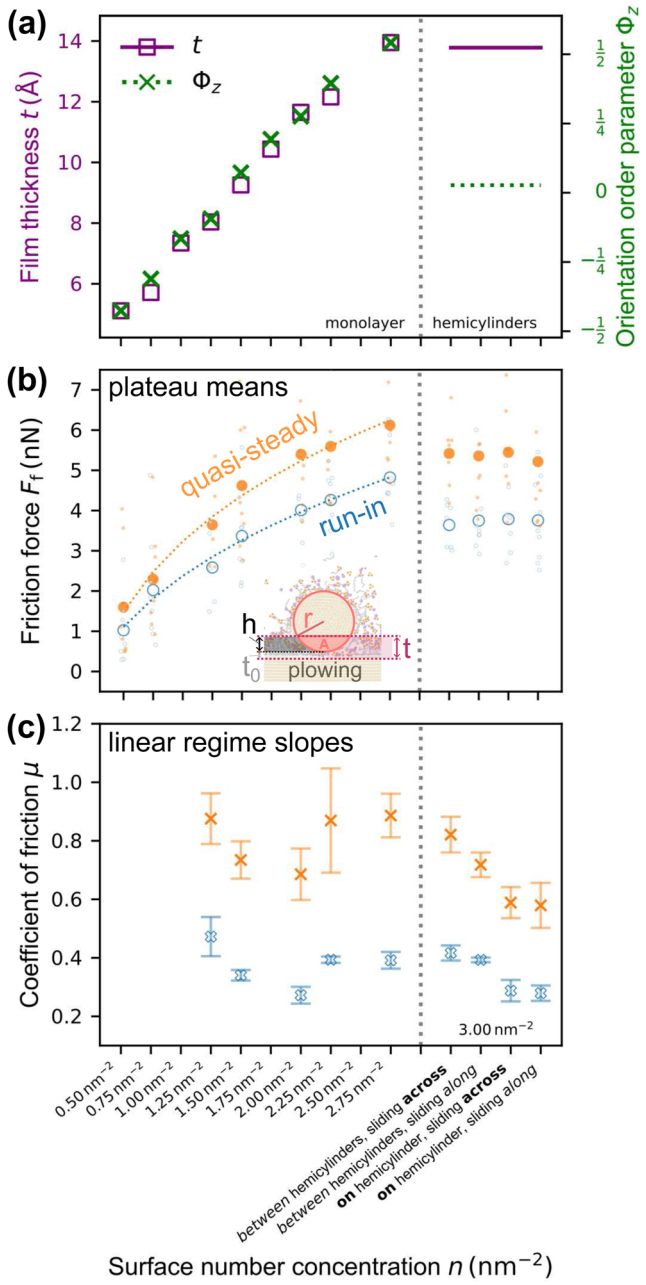

FIG. 8. (a) Thickness t (purple squares and solid line) and orientation order parameter Φ_z (green crosses and dashed line) of undisturbed films at increasing surface concentrations. (b) Averaged friction forces at monomolecular gaps (together with the underlying data points shown as lightly colored circles) for monolayer concentrations up to 2.75 nm^{-2} and for hemicylindrical aggregates at 3 nm^{-2} distinguished by the site and sliding directions. Dashed fits in the monolayer regime of the functional form $a + b\,x^c$ serve to guide the eye. The inset illustrates film thickness t and plowing depth h. (c) Averaged friction coefficients at multimolecular gaps for monolayer concentrations up to 2.75 nm^{-2} and for hemicylindrical aggregates at 3 nm^{-2} distinguished by the site and sliding directions. Markers adhere to the scheme introduced in Figs. 7(b) and 7(c); as before, blue and orange data points correspond to data from the run-in and quasi-steady regimes.

odic box have shown that under the chosen method of fixed normal distance no further relevant information is gained when extending runs beyond that distance, as the system appears run-in after a short sliding distance. To probe a potential directional dependence of the anisotropic hemicylinders, we run these calculations across [solid lines in Figs. 6(a) and 6(b)] and along (dotted lines) the hemicylindrical aggregates. Specifically, Fig. 6 shows results obtained at a fixed normal distance of 3 Å of the tip. The normal force, initially slightly higher for sliding along hemicylinders drops in both cases between a sliding distance of 5 and 10 Å. It stabilizes toward a steady-state around 5 nN for sliding along the hemicylinders but drops into the adhesive regime for sliding across. The friction force is, on average, slightly higher for sliding across than sliding along hemicylinders. In contrast to the normal force, the friction force shows larger absolute fluctuations and increases during the initial run-in period.

In our setup of fixed gap and instantaneous onset of sliding motion, we expect that the initial force response is dominated by the onset of sliding before approaching a (quasi) steady state. In extreme cases, we observe the formation of a bare gold–gold contact, as shown by the dotted line with a negative normal force in Fig. 6(a). In the following analysis, we deliberately exclude all trajectories forming gold–gold contacts and label the first 1 nm of sliding as *run-in*. The subsequent 2 nm are labeled as *quasi-steady*. All our simulations show a similar phenomenology in that we can identify separate run-in and quasi-steady sliding regimes. However, our run-in regime should not be confused with run-in observed for macroscopic contacts.[74]

In the following, we analyze our friction results in these two categories. Specifically, we average normal and friction forces separately over the run-in and quasi-steady sliding segments. Figure 7(a) is a scatter plot of the resulting average friction force vs normal force for all our runs on hemicylinders. For both run-in and quasi-steady sliding, the data evidently exhibit two distinct friction regimes: linear Amonton's friction at lower normal forces and friction that is nearly independent of the normal force at higher loads. The transition from Amonton's to constant force correlates with the transition from two or more molecular layers confined in the contact [see Fig. 7(b) for a snapshot] to only one molecular layer [Fig. 7(c)]. This transition takes place at a normal distance of about 8 Å. Consequently, we categorize data points into *multimolecular* and *monomolecular*, as indicated by crosses and solid symbols, respectively, in Fig. 7(a). The figure also shows corresponding linear fits to the (multimolecular) Amonton's regime as a dotted line, which explicitly goes through the origin. We additionally fit a constant to the monomolecular regime, shown as a solid line.

We have so far focused our detailed analysis on hemicylinders. Now, we extend our considerations to monolayers. In Fig. 8(a), we show the film thickness t and an orientation order parameter Φ_z. We estimate the film thickness t as the mean normal distance between the gold substrate's first atomic layer and the head groups of dodecyl sulfate ions in the adsorption film. The orientation order parameter $\Phi_z = \left(3\langle\cos^2\chi_z\rangle - 1\right)/2$[75] is defined by the angle χ_z between the substrate's surface normal $\hat{z}$ and the gyration tensor-based long principal axis of the dodecyl sulfate ion. In our case, the angular brackets indicate the mean over all molecules in

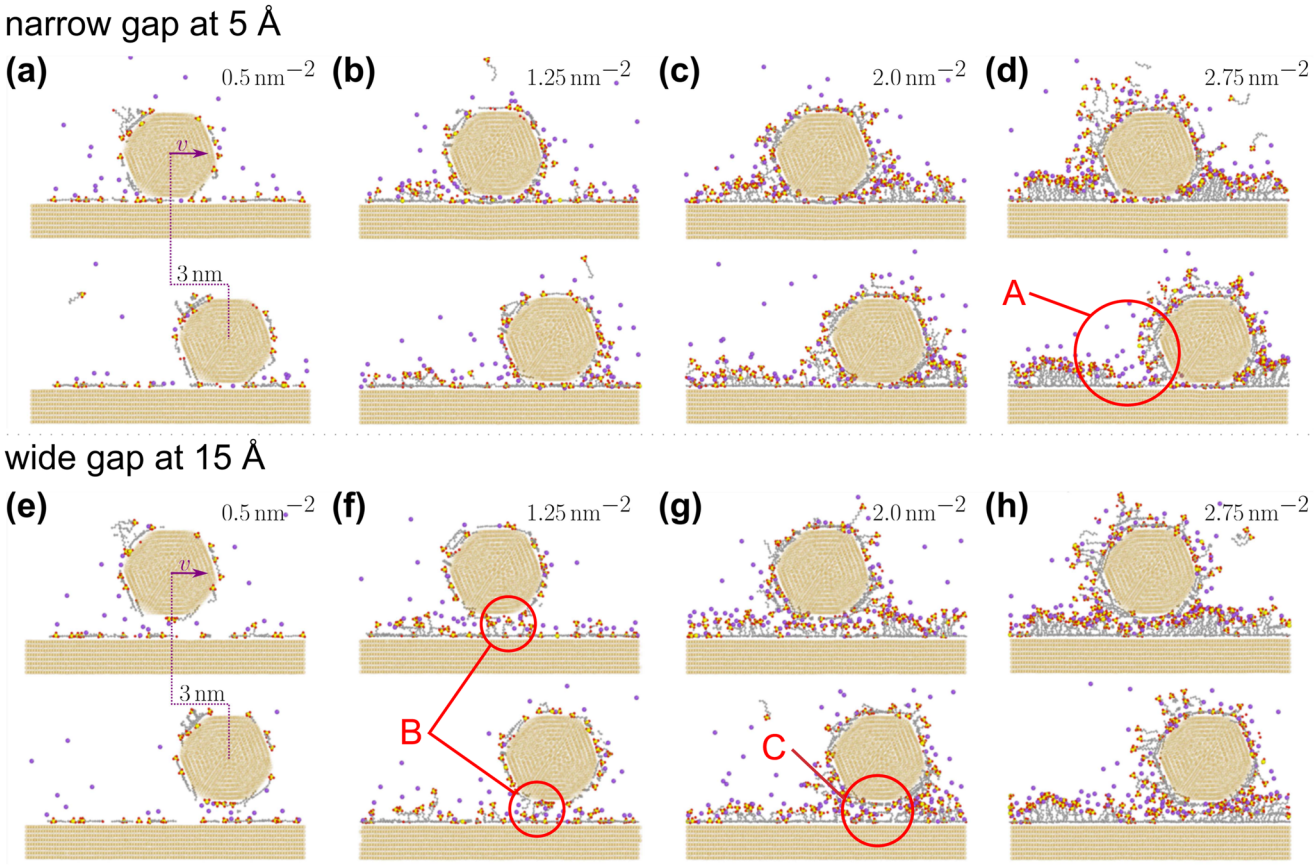

FIG. 9. Cross-sectional snapshots of trajectories at a fixed normal surface–surface distance (a)–(d) 5 Å and (e)–(h) 15 Å before (top) and after (bottom) lateral sliding for 3 nm at velocity $v = 1$ m s^{-1} on monolayers of surface concentrations (a), (e) 0.5 nm^{-2}, (b), (f) 1.25 nm^{-2}, (c), (g) 2.0 nm^{-2}, and (d), (h) 2.75 nm^{-2}. Feature A shows a groove opening up in the track of the probe when plowing into a dense film. Feature B shows monomers adhering to both the probe and the substrate for sparse adsorption films. Feature C shows a well-developed boundary lubrication film without any such bridging chains.

the adsorption film. A value of nearly $-\frac{1}{2}$ at 0.5 nm^{-2} surface concentration indicates anti-alignment with $\hat{z}$. All monomers lie flat on the substrate. Values above 0 mean partial alignment with $\hat{z}$. At high concentrations, the monomers tilt upward. A value of zero indicates a uniform distribution of alignment. This is the case for the fanned chains in hemicylindrical aggregates. Although t and Φ_z show corresponding linear behavior with increasing concentration on monolayers, snapshots in Fig. 9 and the two-dimensional structure factor S evaluated on a thin layer of gold in Fig. 10(a) and on the substrate-adjacent layer of carbon atoms in the dodecyl sulfate ions in Fig. 10 reveal an important change in film morphology with increasing concentrations. At 0.5 nm^{-2}, Fig. 10(b) reveals alignments of flat-lying DS^- with the Au(111) crystal lattice of panel (a). Figures 9(f)–9(h) directly show how chains align with $\hat{z}$ with increasing concentrations. Correspondingly, the characteristic hexagonal pattern of the gold substrate gradually disappears from the structure factor in Figs. 10(c) and 10(d). For hemicylindrical aggregates, the anisotropic ordering of chains is clearly discernible in Fig. 10(e).

The frictional phenomenology described above for hemicylinders also holds for monolayers at lower surface concentrations: The dependence of friction force on normal force splits into linear and quasi-constant regimes. Again, we extract a constant friction force F_f from the normal load-independent regime and Amonton's friction coefficient μ from the linear friction regime for our monolayers in the surface concentration range from 0.5 to 2.75 nm^{-2}. Figure 8(b) shows the saturated mean F_f at high loads and narrow gaps as circles. The small dots show the individual values of the friction force that were averaged to obtain the mean F_f. The friction force in the quasi-steady regime rises monotonically from ~1 nN to ~5 nN with increasing monolayer concentration. Dashed lines in panel (b) show fits of the friction data to an empirical power-law $a + b\,x^c$ with fit parameters a, b, and c. The run-in regime follows this trend, albeit at lower F_f. Note that the plot also shows the results obtained for hemicylinders at a surface concentration of 3 nm^{-2}, where we separately report friction force for the two sliding directions. Normal forces in this regime do not exceed 20 nN and their concentration-wise averages mostly fall in the range of 5 to 10 nN for the quasi-steady

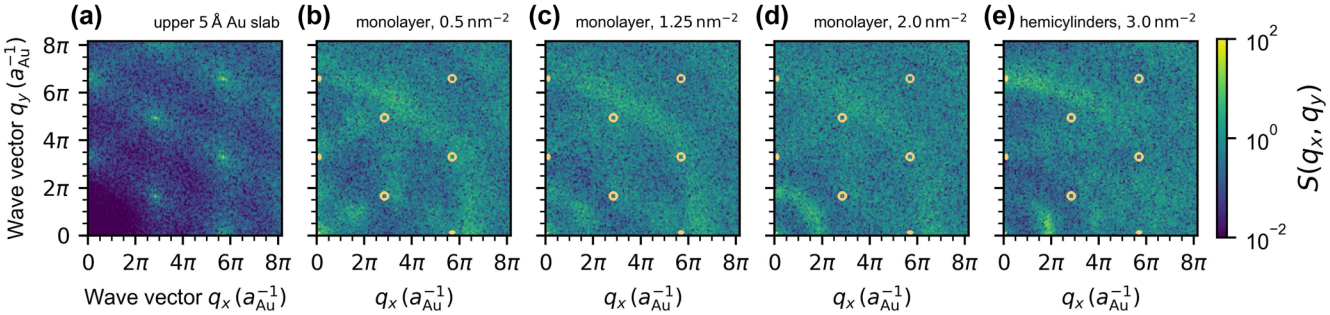

FIG. 10. Two-dimensional structure factor $S(q_x, q_y)$ with wave vector q_x and q_y in units of the reciprocal gold lattice constant a_{Au}^{-1} on (a) the gold substrate's atomic layers in an upper 5 Å slab and on the DS^- ion's carbon atoms in the single atomic layer adjacent to the gold substrate for (b)–(d) select monolayers of increasing concentration and for (e) hemicylinders. Yellow circles in panels (b)–(e) show the peaks of the structure factor of the underlying gold substrate in panel (a).

regime. With an area A ≈ 3.4 nm^2 of the probe's downward-facing Au(111) facet, this means an upper limit of about 3 GPa for pressure within the gap.

Hemicylinders show a slightly lower F_f of ~4.5 nN than monolayers at the highest surface concentration. When sliding on hemicylinders, the different starting configurations and sliding directions do not appear to systematically differ [see Fig. 8(b)]. This means that the orientation of the hemicylinders does not introduce anisotropy into the frictional response. If any, there is a slight systematic difference in the mean quasi-steady friction force from sliding across to sliding along the hemicylinders. Prominent is the drop of the plateau friction force from the dense monolayer at 2.75 nm^{-2} to hemicylindrical aggregates at 3 nm^{-2}.

Similarly, Fig. 8(c) shows the friction coefficient μ at low normal forces, where Amonton's friction law holds. The friction coefficient μ does not have a clear monotonic trend. In the quasi-steady regime [filled markers in Fig. 8(c)], we see a decrease of μ from 0.9 at 1.25 nm^{-2} to a minimum of 0.7 at 2 nm^{-2}, followed by a subsequent increase back to 0.9. For the hemicylindrical configurations, we observe μ of 0.8 and 0.7 for sliding across and along the hemicylinders for initial placement of the probe in a valley between the two aggregates. For an initial placement centered on the apex of an aggregate, μ decreases to 0.6. Qualitatively similar behavior is observable for the run-in regime [unfilled markers in Fig. 8(c)], with overall lower friction coefficients. During run-in, the values of μ vary between 0.3 and 0.5 in the monolayer case. For hemicylinders, it is ~0.4 for a probe initially placed between the hemicylinders and ~0.3 for the initial placement on a hemicylindrical aggregate.

Figure 9 shows snapshots of the initial and final configurations for a few select sliding trajectories that underlie the presented analysis. Panels (a)–(d) show sliding at a narrow gap of 5 Å, where only a single molecular layer is confined between the probe and the substrate. The surface coverage increases from left to right. Such trajectories are representative of cases where Amonton's law does not hold. Figures 9(e) and 9(f) show sliding at a wider gap of 15 Å, where multiple molecular layers can be accommodated between the probe and the substrate. Such trajectories are representative of the Amonton's friction regime.

DISCUSSION

The term interfacial friction has been suggested to distinguish the sliding of two molecularly smooth, undamaged surfaces, possibly lubricated by one or two molecular layers, from boundary lubrication, which implies plastic deformation and asperity contact on rough surfaces.[76] Clearly, the sliding of atomically smooth surfaces of the tip and the substrate, lubricated by the individual flat-lying molecules of varying surface concentrations at narrow gaps, falls into the category of interfacial friction. Other molecular dynamics simulations consistently show Amonton's behavior in the interfacial friction regime.[77] In all our simulations, friction forces become independent of normal forces at narrow gaps that accommodate a single molecular layer at most. At such close distances, there is a competition of adhesive gold–gold interaction[52] and repulsion by compressed substrate and confined molecules. This leads to a wide range of net normal forces across the narrow range of surface–surface distances below 8 Å with little variation in mean lateral forces.

Friction felt by the probe must be made up by viscous drag in the solvent, plowing into the surfactant film, and *cobblestone*-like sliding on the atomistic scale, where the atomic granularity of gold surface lattices and trapped surfactant molecules plays significantly into friction.[78] Friction forces oscillate at the order of Ångstrom during lateral sliding in Fig. 6(b), indicative of the cobblestone mechanism and pointing to the Au(111) facets' lattice with a nearest neighbor distance of ~2.88 Å. The friction force in Fig. 2(b) shows that these oscillations disappear at surface–surface distances larger than a few angstroms.

In Fig. 8(b), we observe a sublinear friction force vs concentration relationship toward the upper end of the investigated concentration range at narrow gaps. At sparse surface coverage with flat-lying monomers (concentrations below 1 nm^{-2}), the probe moves across the film laterally only subject to the viscous drag of water and the discussed cobblestone contribution. For higher concentrations, the probe has indented the surfactant aggregates normally and plows into the adsorption film laterally, opening up a groove at its tail as illustrated by feature marker A in Fig. 9(d). The structure factor of substrate-adjacent monomers in Fig. 10(e) shows

that in the case of hemicylindrical aggregates, many monomers are lying flat on the gold substrate, not unlike the flat-lying monolayers at lower concentrations, but well aligned along the cylinder axis. They form the foundation of hemicylindrical domes assembled above. At narrow gaps, the probe slides across this foundational monolayer while simply peeling off the surfactant domes. Snapshots of Figs. 9(g) and 9(h) and the absence of any ordering in the structure factors of Fig. 10(d) reveals that there is no such foundational layer of flat-lying monomers in the case of the densely packed monolayer, and consequently, no simple peel-off is possible.

Since we have not investigated the velocity dependence in our lateral sliding simulations, we cannot decide to what extent the plowing probe experiences velocity-dependent viscous drag or velocity-independent resistance due to the elastoplastic deformation of the film. Experiments have shown SDS adsorption films to start behaving viscous around a surface coverage of 2 nm^{-2}.[79] In the earliest plowing models for soft metals, friction force $F_f = F_s + F_p$ is the sum of F_s, the force required to shear the metallic junctions, and $F_p = Ap_Y$, the force required to displace the softer metal from the path of the slider,[80] where A is the cross-sectional area of the plowing track and p_Y the pressure to cause plastic flow of the softer metal, its indentation hardness. We use this simple model for an order-of-magnitude estimate of the adsorption film's flow stress p_Y. The plowing depth amounts to $h = t - t_0$ as illustrated by the inset in Fig. 8(b). Neglecting viscous drag in water, we relate the discussed cobblestone contribution in our systems to F_s and the displacement of surfactant molecules in the plowing track to F_p. This approach leads to an estimated mean p_Y at the order of 1 GPa for the range from 1.0 to 2.75 nm^{-2}.

For wider gaps, plowing friction plays a reduced, vanishing, role. Gold–gold adhesion and cobblestone oscillations disappear. We enter a regime of well-behaved boundary lubrication where the adsorption films on the probe and the substrate remain largely intact, as seen in Figs. 9(e)–9(h). Studies on bare probes penetrating chemisorbed monolayers[37,81] or symmetric boundary-lubricated flat-on-flat systems[82] report adhesive effects and introduce the Derjaguin offset F_0 as a modification to Amonton's law, $F_f = \mu F_N + F_0$. In our model of the probe and the substrate covered with physisorbed anionic surfactant molecules, we have not observed any net adhesive interaction in the normal approach curves. Accordingly, none of our friction force–normal force relations exhibits a considerable finite intercept. We observe Amonton's friction $F_f = \mu F_N$, as illustrated with cross markers and dashed linear fits in Fig. 7.

Other than the monotonically increasing saturated friction forces at narrow gaps in Fig. 8(b), the concentration-dependent friction coefficient at wide gaps in Fig. 8(c) clearly shows a minimum for both run-in and quasi-steady regime in the concentration range of 1.5–2.0 nm^{-2} for a monolayer. To understand the minimum in the monolayer case, we discuss Figs. 9(f)–9(h) together with the corresponding friction coefficients at concentrations of 1.25, 2.0, and 2.75 nm^{-2} in Fig. 8(c). In Fig. 9(f) at 1.25 nm^{-2}, sparse coverage with flat-lying monomers at the probe and the substrate may introduce single monomers bridging the gap, emphasized by feature marker B. In Fig. 9(g) at 2.0 nm^{-2}, denser coverage leads to a well-formulated lubrication layer pointed out by marker C. In Fig. 9(g) at 2.75 nm^{-2}, very dense coverage introduces a slight plowing contribution again.

For hemicylinders, the friction coefficient shows a clear site dependence. Beginning to slide on a hemicylindrical aggregate yields lower friction than beginning to slide in the middle between the two aggregates. This low friction coefficient reaches the monolayer minimum and even exceeds it in the case of the quasi-steady regime. To explain the difference in friction coefficients for an initial configuration centered between the two hemicylindrical aggregates and a starting configuration on top of an aggregate, we rely on similar arguments. The former starting position means a groove for the probe to embed in and an increased likelihood of hydrophobic attraction between hydrocarbon tails, similar to the case of low monolayer concentrations. The latter starting position means densely packed monomer layering to bear the probe, similar to the case of higher monolayer concentrations.

In macroscopic friction tests, higher adsorption mass is usually associated with improved lubrication. This appears to be the case for SDS adsorption films on different base materials,[4,6,9,10] which show a decreased kinetic friction coefficient with increasing adsorption mass as long as the film does not yet transition to the hemicylinder phase. In our microscopic model with a sharp probe, however, we observe exactly the inverse of this trend for the normal force-independent response at narrow gaps in Fig. 8(b). Consistent with our observation, Nalam *et al.*[83] have experimentally shown the increase of friction with increasing adsorption film density for fatty acids probed with a sharp AFM tip. Similarly, Gao *et al.*[37] have elucidated the relation between probe curvature, film density, and friction under plowing into such organic friction modifier (OFM) monolayers using MD simulations. The higher the concentration and the sharper the probe, the more prominent the plowing effect and, hence, the higher the friction coefficient in constant normal force simulations.

In the regime of Amonton's friction, we observe a minimum in the concentration-dependent friction coefficient that arises due to the complex interplay between the adhesive and repulsive normal forces and plowing into the adsorption film. A minimum in the concentration-dependent coefficient of friction on SDS adsorption films on stainless steel has indeed been observed in macroscopic ball-on-flat experiments.[6,11] In the image of Bowden's model for boundary lubrication,[84,85] a breakdown of the lubricant film leads to metallic junctions that contribute to the friction force. It has been argued that an SDS adsorption film in the monolayer phase prevents the formation of such junctions, improving lubrication with increasing concentration, whereas the transition to hemicylindrical stripe-like aggregates at again higher concentrations exposes bare metal substrate between the stripes and hence facilitates junction formation, promoting stick-slip.[6]

Typical ball-on-flat experiments, such as those of Ref. 6, have rough interfaces and run at velocities on the order of mm s^{-1} and at nominal pressures below 1GPa. For rough contacts, the pressure on individual asperities follows a double-Gaussian distribution with a long tail (see, e.g., Refs. 86 and 87). This means that individual asperities can experience pressures orders of magnitude higher than the nominal Hertzian pressure pushing the interfaces together. Pressures of several GPa in the single-asperity contact of our simulations are therefore representative for such a multi-asperity contact. We note that, nevertheless, our single asperity friction simulation appears to indicate a friction minimum at a concentration range that

coincides with the minimum of friction observed in macroscopic experiments.[6]

SUMMARY AND CONCLUSION

We showed that MD-simulated AFM force–distance curves and sliding measurements exhibit morphology-dependent characteristics. For this purpose, we moved a 5 nm model gold AFM tip (or model asperity) normally onto or laterally along a $15 \times 15 \times 15$ nm^3 gold substrate block. All probe facets and the contacting substrate surface were covered by SDS adsorption films of equivalent density to mimic a nanotribological system in the absence of any externally applied potential bias between the two contacting bodies that are facing each other with Au(111) planes. Specifically, we investigated preassembled monolayers at surface concentrations from 0.5 nm^{-2} to 2.75 nm^{-2} and hemicylindrical aggregates at 3.0 nm^{-2}.

In short, we have highlighted the impact of different parametric dimensions, namely probe velocity, surfactant concentration, film morphology, and probing site on the characteristic features of force–distance curves. In our lateral sliding simulations, we have been able to draw statistically reliable conclusions upon the manifestation of plowing friction and boundary lubrication on intact film layers in a nanotribological system by the evaluation of a large number of trajectories. Friction forces saturate around a nearly normal force-independent plateau at narrow gaps and high normal force. At very close distances, a cobblestone-contribution induced by the Au(111) facets' atomic lattices arises in the friction signal. In this regime, the probe plows deeply into the dense adsorption film. In agreement with classical plowing models, this leads to increased friction with increased film density, an inversion of the expectation of improved lubrication with increased adsorption mass in macroscopic friction experiments expected for sharp asperities. At intermediate probe–substrate distances and moderate normal load, our systems adhere to Amonton's law without any adhesive contribution. Coefficients of friction range from 0.3 to 0.9, depending on the morphology, site, and concentration. The contact resembles a boundary-lubricated friction couple with intact adsorption layers within this regime. The concentration-dependent monolayer friction coefficient reaches a minimum of around 1.5–2 nm^{-2}, which we attribute to the complex interplay of hydrophobic attraction, the film's repulsion under compression, and the onset of plowing. Similar mechanisms can explain the site and sliding direction dependency of the hemicylinders friction coefficient as well.

ACKNOWLEDGMENTS

We used LAMMPS[88] for all molecular dynamics simulations. Adsorption films were packed with PACKMOL.[89] Preparatory molecular dynamics runs have been carried out with GROMACS.[90] Probe and substrate systems were merged with the help of VMD[91] and its PBCTOOLS, TOPOTOOLS,[92] and MERGETOOLS plugins. Simulation runs were orchestrated with FIREWORKS[93] and DTOOL.[94] Rendered images have been produced with OVITO.[95] Simulations were carried out on NEMO at the University of Freiburg (Deutsche Forschungsgemeinschaft Grant No. INST 39/963-1 FUGG) and on JUWELS at the Jülich Supercomputing Center (Project Nos. hfr13 and hfr21). Data are stored on bwSFS (University of Freiburg, Deutsche Forschungsgemeinschaft Grant No. INST 39/1099-1 FUGG).

AUTHOR DECLARATIONS

Conflict of Interest

The authors have no conflicts to disclose.

Author Contributions

Johannes L. Hörmann: Conceptualization (equal); Data curation (equal); Investigation (equal); Methodology (equal); Writing – original draft (equal); Writing – review & editing (equal). **Chenxu Liu**: Data curation (equal); Investigation (equal); Writing – review & editing (equal). **Yonggang Meng**: Conceptualization (equal); Funding acquisition (equal); Resources (equal); Supervision (equal); Writing – review & editing (equal). **Lars Pastewka**: Conceptualization (equal); Methodology (equal); Resources (equal); Supervision (equal); Writing – review & editing (equal).

DATA AVAILABILITY

The data that support the findings of this study are available from the corresponding author upon reasonable request.

REFERENCES

[1] M. Jaschke, H.-J. Butt, H. E. Gaub, and S. Manne, "Surfactant aggregates at a metal surface," Langmuir **13**, 1381 (1997).
[2] M. Chen, I. Burgess, and J. Lipkowski, "Potential controlled surface aggregation of surfactants at electrode surfaces – A molecular view," Surf. Sci. **603**, 1878 (2009).
[3] I. Burgess, C. A. Jeffrey, X. Cai, G. Szymanski, Z. Galus, and J. Lipkowski, "Direct visualization of the potential-controlled transformation of hemimicellar aggregates of dodecyl sulfate into a condensed monolayer at the Au(111) electrode surface," Langmuir **15**, 2607 (1999).
[4] J. Zhang and Y. Meng, "Boundary lubrication by adsorption film," Friction **3**, 115 (2015).
[5] X. Yang, Y. Meng, and Y. Tian, "Potential-controlled boundary lubrication of stainless steels in non-aqueous sodium dodecyl sulfate solutions," Tribol. Lett. **53**, 17 (2014).
[6] J. Zhang and Y. Meng, "Stick–slip friction of stainless steel in sodium dodecyl sulfate aqueous solution in the boundary lubrication regime," Tribol. Lett. **56**, 543 (2014).
[7] J. Zhang, Y. Meng, Y. Tian, and X. Zhang, "Effect of concentration and addition of ions on the adsorption of sodium dodecyl sulfate on stainless steel surface in aqueous solutions," Colloids Surf., A **484**, 408 (2015).
[8] J. Zhang, Y. Meng, and X. Yu, "Control of friction distribution on stainless steel surface in sodium dodecyl sulfate aqueous solution by bipolar electrochemistry," Tribol. Lett. **59**, 43 (2015).
[9] C. Liu, J. Fang, X. Wen, Y. Tian, and Y. Meng, "Active control of boundary lubrication of ceramic tribo-pairs in sodium dodecyl sulfate aqueous solutions," Tribol. Lett. **69**, 144 (2021).
[10] C. Liu, X. Li, X. Li, W. Li, Y. Tian, and Y. Meng, "On-line feedback control of sliding friction of metals lubricated by adsorbed boundary SDS films," Lubricants **10**, 148 (2022).
[11] C. Liu, Y. Tian, Z. A. Khan, and Y. Meng, "Mitigation of tribocorrosion of metals in aqueous solutions by potential-enhanced adsorption of surfactants," Friction **11**, 801 (2023).

[12]P. Mukerjee and K. J. Mysels, "Critical micelle concentrations of aqueous surfactant systems," National Bureau of Standards Report No. RSRDS-NBS 36, 1971.
[13]M. Miura and M. Kodama, "The second CMC of the aqueous solution of sodium dodecyl sulfate. I. Conductivity," Bull. Chem. Soc. Jpn. **45**, 428 (1972).
[14]M. Kodama and M. Miura, "The second CMC of the aqueous solution of sodium dodecyl sulfate. II. Viscosity and density," Bull. Chem. Soc. Jpn. **45**, 2265 (1972).
[15]M. Kodama, Y. Kubota, and M. Miura, "The second CMC of the aqueous solution of sodium dodecyl sulfate. III. Light-scattering," Bull. Chem. Soc. Jpn. **45**, 2953 (1972).
[16]Y. Kubota, M. Kodama, and M. Miura, "The second CMC of an aqueous solution of sodium dodecyl sulfate. IV. Fluorescence depolarization," Bull. Chem. Soc. Jpn. **46**, 100 (1973).
[17]V. Y. Bezzobotnov, S. Borbely, L. Cser, B. Farago, I. A. Gladkih, Y. M. Ostanevich, and S. Vass, "Temperature and concentration dependence of properties of sodium dodecyl sulfate micelles determined from small angle neutron scattering experiments," J. Phys. Chem. **92**, 5738 (1988).
[18]P. Kékicheff, C. Grabielle-Madelmont, and M. Ollivon, "Phase diagram of sodium dodecyl sulfate-water system: 1. A calorimetric study," J. Colloid Interface Sci. **131**, 112 (1989).
[19]B. L. Bales, L. Messina, A. Vidal, M. Peric, and O. R. Nascimento, "Precision relative aggregation number determinations of SDS micelles using a spin probe. A model of micelle surface hydration," J. Phys. Chem. B **102**, 10347 (1998).
[20]N. J. Turro and A. Yekta, "Luminescent probes for detergent solutions. A simple procedure for determination of the mean aggregation number of micelles," J. Am. Chem. Soc. **100**, 5951 (1978).
[21]E. J. Wanless and W. A. Ducker, "Organization of sodium dodecyl sulfate at the graphite-solution interface," J. Phys. Chem. **100**, 3207 (1996).
[22]E. J. Wanless, T. W. Davey, and W. A. Ducker, "Surface aggregate phase transition," Langmuir **13**, 4223 (1997).
[23]E. J. Wanless and W. A. Ducker, "Weak influence of divalent ions on anionic surfactant surface-aggregation," Langmuir **13**, 1463 (1997).
[24]P. M. Karlsson, A. E. C. Palmqvist, and K. Holmberg, "Adsorption of sodium dodecyl sulfate and sodium dodecyl phosphate on aluminum, studied by QCM-D, XPS, and AAS," Langmuir **24**, 13414 (2008).
[25]I. Burgess, V. Zamlynny, G. Szymanski, J. Lipkowski, J. Majewski, G. Smith, S. Satija, and R. Ivkov, "Electrochemical and neutron reflectivity characterization of dodecyl sulfate adsorption and aggregation at the gold–water interface," Langmuir **17**, 3355 (2001).
[26]M. Petri and D. M. Kolb, "Nanostructuring of a sodium dodecyl sulfate-covered Au(111) electrode," Phys. Chem. Chem. Phys. **4**, 1211 (2002).
[27]D. M. Soares, W. E. Gomes, and M. A. Tenan, "Sodium dodecyl sulfate adsorbed monolayers on gold electrodes," Langmuir **23**, 4383 (2007).
[28]H. C. Schniepp, H. C. Shum, D. A. Saville, and I. A. Aksay, "Surfactant aggregates at rough solid-liquid interfaces," J. Phys. Chem. B **111**, 8708 (2007).
[29]S. He, Y. Meng, and Y. Tian, "Correlation between adsorption/desorption of surfactant and change in friction of stainless steel in aqueous solutions under different electrode potentials," Tribol. Lett. **41**, 485 (2011).
[30]A. J. Glover, D. H. Adamson, and H. C. Schniepp, "Charge-driven selective adsorption of sodium dodecyl sulfate on graphene oxide visualized by atomic force microscopy," J. Phys. Chem. C **116**, 20080 (2012).
[31]M. T. Knippenberg, P. T. Mikulski, B. I. Dunlap, and J. A. Harrison, "Atomic contributions to friction and load for tip–self-assembled monolayers interactions," Phys. Rev. B **78**, 235409 (2008).
[32]M. Chandross, C. D. Lorenz, M. J. Stevens, and G. S. Grest, "Simulations of nanotribology with realistic probe tip models," Langmuir **24**, 1240 (2008).
[33]J. P. Ewen, C. Gattinoni, N. Morgan, H. A. Spikes, and D. Dini, "Nonequilibrium molecular dynamics simulations of organic friction modifiers adsorbed on iron oxide surfaces," Langmuir **32**, 4450 (2016).
[34]J. P. Ewen, D. M. Heyes, and D. Dini, "Advances in nonequilibrium molecular dynamics simulations of lubricants and additives," Friction **6**, 349 (2018).
[35]S. de Beer and M. H. Müser, "Alternative dissipation mechanisms and the effect of the solvent in friction between polymer brushes on rough surfaces," Soft Matter **9**, 7234 (2013).
[36]S. de Beer, E. Kutnyanszky, P. M. Schön, G. J. Vancso, and M. H. Müser, "Solvent-induced immiscibility of polymer brushes eliminates dissipation channels," Nat. Commun. **5**, 3781 (2014).
[37]H. Gao, J. P. Ewen, R. Hartkamp, M. H. Müser, and D. Dini, "Scale-dependent friction–coverage relations and nonlocal dissipation in surfactant monolayers," Langmuir **37**, 2406 (2021).
[38]G. Sauerbrey, "Verwendung von Schwingquarzen zur Wägung dünner Schichten und zur Mikrowägung," Z. Phys. **155**, 206 (1959).
[39]J. Thavorn, J. J. Hamon, B. Kitiyanan, A. Striolo, and B. P. Grady, "Competitive surfactant adsorption of AOT and Tween 20 on gold measured using a quartz crystal microbalance with dissipation," Langmuir **30**, 11031 (2014).
[40]R. A. Heising, *Quartz Crystals for Electrical Circuits: Their Design and Manufacture*, *The Bell Telephone Laboratories Series* (Van Nostrand, New York, 1946).
[41]J. P. Ewen, C. Gattinoni, F. M. Thakkar, N. Morgan, H. A. Spikes, and D. Dini, "A comparison of classical force-fields for molecular dynamics simulations of lubricants," Materials **9**, 651 (2016).
[42]B. Roux, "Theoretical study of ion transport in the gramicidin a channel - NASA/ADS," Ph.D. thesis, Harvard University, 1990.
[43]A. D. MacKerell, J. Wiorkiewicz-Kuczera, and M. Karplus, "An all-atom empirical energy function for the simulation of nucleic acids," J. Am. Chem. Soc. **117**, 11946 (1995).
[44]M. Schlenkrich, J. Brickmann, A. D. MacKerell, and M. Karplus, "An empirical potential energy function for phospholipids: Criteria for parameter optimization and applications," in *Biological Membranes: A Molecular Perspective from Computation and Experiment*, edited by K. M. Merz and B. Roux (Birkhäuser, Boston, MA, 1996), pp. 31–81.
[45]A. D. Mackerell, Jr., D. Bashford, M. Bellott, R. L. Dunbrack, J. D. Evanseck, M. J. Field, S. Fischer, J. Gao, H. Guo, S. Ha, D. Joseph-McCarthy, L. Kuchnir, K. Kuczera, F. T. K. Lau, C. Mattos, S. Michnick, T. Ngo, D. T. Nguyen, B. Prodhom, W. E. Reiher, B. Roux, M. Schlenkrich, J. C. Smith, R. Stote, J. Straub, M. Watanabe, J. Wiórkiewicz-Kuczera, D. Yin, and M. Karplus, "All-atom empirical potential for molecular modeling and dynamics studies of proteins," J. Phys. Chem. B **102**, 3586 (1998).
[46]N. Yoshii and S. Okazaki, "A molecular dynamics study of surface structure of spherical SDS micelles," Chem. Phys. Lett. **426**, 66 (2006).
[47]N. Yoshii, K. Iwahashi, and S. Okazaki, "A molecular dynamics study of free energy of micelle formation for sodium dodecyl sulfate in water and its size distribution," J. Chem. Phys. **124**, 184901 (2006).
[48]N. Yoshii and S. Okazaki, "A molecular dynamics study of structural stability of spherical SDS micelle as a function of its size," Chem. Phys. Lett. **425**, 58 (2006).
[49]X. Tang, P. H. Koenig, and R. G. Larson, "Molecular dynamics simulations of sodium dodecyl sulfate micelles in water—the effect of the force field," J. Phys. Chem. B **118**, 3864 (2014).
[50]H. Heinz, T.-J. Lin, R. Kishore Mishra, and F. S. Emami, "Thermodynamically consistent force fields for the assembly of inorganic, organic, and biological nanostructures: The INTERFACE force field," Langmuir **29**, 1754 (2013).
[51]R. B. Best, X. Zhu, J. Shim, P. E. M. Lopes, J. Mittal, M. Feig, and A. D. MacKerell, "Optimization of the additive CHARMM all-atom protein force field targeting improved sampling of the backbone ϕ, ψ and side-chain $\chi 1$ and $\chi 2$ dihedral angles," J. Chem. Theory Comput. **8**, 3257 (2012).
[52]G. Grochola, S. P. Russo, and I. K. Snook, "On fitting a gold embedded atom method potential using the force matching method," J. Chem. Phys. **123**, 204719 (2005).
[53]P. J. Steinbach and B. R. Brooks, "New spherical-cutoff methods for long-range forces in macromolecular simulation," J. Comput. Chem. **15**, 667 (1994).
[54]B. R. Brooks, C. L. Brooks, A. D. Mackerell, L. Nilsson, R. J. Petrella, B. Roux, Y. Won, G. Archontis, C. Bartels, S. Boresch, A. Caflisch, L. Caves, Q. Cui, A. R. Dinner, M. Feig, S. Fischer, J. Gao, M. Hodoscek, W. Im, K. Kuczera, T. Lazaridis, J. Ma, V. Ovchinnikov, E. Paci, R. W. Pastor, C. B. Post, J. Z. Pu, M. Schaefer, B. Tidor, R. M. Venable, H. L. Woodcock, X. Wu, W. Yang, D. M. York, and

M. Karplus, "CHARMM: The biomolecular simulation program," J. Comput. Chem. **30**, 1545 (2009).
[55]R. W. Hockney and J. W. Eastwood, *The Particle-Mesh Force Calculation*, *Computer Simulation Using Particles* (Adam Hilger, Bristol and New York, NY, 1989), p. 120.
[56]R. D. Groot and P. B. Warren, "Dissipative particle dynamics: Bridging the gap between atomistic and mesoscopic simulation," J. Chem. Phys. **107**, 4423 (1997).
[57]T. Soddemann, B. Dünweg, and K. Kremer, "Dissipative particle dynamics: A useful thermostat for equilibrium and nonequilibrium molecular dynamics simulations," Phys. Rev. E **68**, 046702 (2003).
[58]B. Rai and Pradip, "Modeling self-assembly of surfactants at interfaces," Curr. Opin. Chem. Eng. **15**, 84 (2017).
[59]G. Bussi, T. Zykova-Timan, and M. Parrinello, "Isothermal-isobaric molecular dynamics using stochastic velocity rescaling," J. Chem. Phys. **130**, 074101 (2009).
[60]H. J. C. Berendsen, J. P. M. Postma, W. F. Van Gunsteren, A. DiNola, and J. R. Haak, "Molecular dynamics with coupling to an external bath," J. Chem. Phys. **81**, 3684 (1984).
[61]T. Schneider and E. Stoll, "Molecular-dynamics study of a three-dimensional one-component model for distortive phase transitions," Phys. Rev. B **17**, 1302 (1978).
[62]S. Nosé, "A molecular dynamics method for simulations in the canonical ensemble," Mol. Phys. **52**, 255 (1984).
[63]W. G. Hoover, "Canonical dynamics: Equilibrium phase-space distributions," Phys. Rev. A **31**, 1695 (1985).
[64]P. A. Thompson and M. O. Robbins, "Origin of stick-slip motion in boundary lubrication," Science **250**, 792 (1990).
[65]C. M. Mate and R. W. Carpick, *Tribology on the Small Scale: A Modern Textbook on Friction, Lubrication, and Wear*, 2nd ed. (Oxford University Press, Oxford, 2019).
[66]M. A. González and J. L. F. Abascal, "The shear viscosity of rigid water models," J. Chem. Phys. **132**, 096101 (2010).
[67]J. Hörmann and L. Pastewka, SDS adsorptions films at the H_2O – Au(111) interface: Molecular dynamics study of AFM tip–surface contact," *NIC Series, Publications Series of the John von Neumann Institute for Computing (NIC)* (Forschungszentrum Jülich, Jülich, Germany, 2020), Vol. 50, pp. 101–107.
[68]J. Hensman, N. Fusi, and N. D. Lawrence "Gaussian processes for big data," in *Proceedings of the Twenty-ninth Conference On Uncertainty In Artificial Intelligence, UAI'13* (AUAI Press, 2013), pp. 282–290.
[69]D. G. Krige, "A statistical approach to some basic mine valuation problems on the Witwatersrand," J. South. Afr. Inst. Min. Metall. **52**, 119 (1951).
[70]M.-D. Krass, G. Krämer, U. Dellwo, and R. Bennewitz, "Molecular layering in nanometer-confined lubricants," Tribol. Lett. **66**, 87 (2018).
[71]J. N. Israelachvili and P. M. McGuiggan, "Forces between surfaces in liquids," Science **241**, 795 (1988).
[72]S. J. O'Shea, N. N. Gosvami, L. T. W. Lim, and W. Hofbauer, "Liquid atomic force microscopy: Solvation forces, molecular order, and squeeze-out," Jpn. J. Appl. Phys. **49**, 08LA01 (2010).
[73]J. N. Israelachvili, *Intermolecular and Surface Forces* (Academic Press, London, 1991).
[74]P. J. Blau, "On the nature of running-in," Tribol. Int. **38**, 1007 (2005).
[75]A. Seelig and J. Seelig, "Dynamic structure of fatty acyl chains in a phospholipid bilayer measured by deuterium magnetic resonance," Biochemistry **13**, 4839 (1974).
[76]J. N. Israelachvili, "Adhesion, friction and lubrication of molecularly smooth surfaces," in *Fundamentals of Friction: Macroscopic and Microscopic Processes, NATO ASI Series*, edited by I. L. Singer and H. M. Pollock (Springer, Dordrecht, Netherlands, 1992), pp. 351–385.
[77]G. He, M. H. Müser, and M. O. Robbins, "Adsorbed layers and the origin of static friction," Science **284**, 1650 (1999).
[78]A. M. Homola, J. N. Israelachvili, M. L. Gee, and P. M. McGuiggan, "Measurements of and relation between the adhesion and friction of two surfaces separated by molecularly thin liquid films," J. Tribol. **111**, 675 (1989).
[79]A. M. Poskanzer and F. C. Goodrich, "Surface viscosity of sodium dodecyl sulfate solutions with and without added dodecanol," J. Phys. Chem. **79**, 2122 (1975).
[80]F. P. Bowden, A. J. W. Moore, and D. Tabor, "The ploughing and adhesion of sliding metals," J. Appl. Phys. **14**, 80 (1943).
[81]A. Z. Summers, C. R. Iacovella, P. T. Cummings, and C. MCabe, "Investigating alkylsilane monolayer tribology at a single-asperity contact with molecular dynamics simulation," Langmuir **33**, 11270 (2017).
[82]S. J. Eder, A. Vernes, and G. Betz, "On the Derjaguin offset in boundary-lubricated nanotribological systems," Langmuir **29**, 13760 (2013).
[83]P. C. Nalam, A. Pham, R. V. Castillo, and R. M. Espinosa-Marzal, "Adsorption behavior and nanotribology of amine-based friction modifiers on steel surfaces," J. Phys. Chem. C **123**, 13672 (2019).
[84]F. P. Bowden and L. Leben, "The friction of lubricated metals," Philos. Trans. R. Soc. A **239**, 1 (1940).
[85]F. P. Bowden, J. N. Gregory, and D. Tabor, "Lubrication of metal surfaces by fatty acids," Nature **156**, 97 (1945).
[86]B. N. J. Persson, "Theory of rubber friction and contact mechanics," J. Chem. Phys. **115**, 3840 (2001).
[87]S. Hyun, L. Pei, J.-F. Molinari, and M. O. Robbins, "Finite-element analysis of contact between elastic self-affine surfaces," Phys. Rev. E **70**, 026117 (2004).
[88]A. P. Thompson, H. M. Aktulga, R. Berger, D. S. Bolintineanu, W. M. Brown, P. S. Crozier, P. J. in 't Veld, A. Kohlmeyer, S. G. Moore, T. D. Nguyen, R. Shan, M. J. Stevens, J. Tranchida, C. Trott, and S. J. Plimpton, "LAMMPS - A flexible simulation tool for particle-based materials modeling at the atomic, meso, and continuum scales," Comput. Phys. Commun. **271**, 108171 (2022).
[89]L. Martínez, R. Andrade, E. G. Birgin, and J. M. Martínez, "PACKMOL: A package for building initial configurations for molecular dynamics simulations," J. Comput. Chem. **30**, 2157 (2009).
[90]M. J. Abraham, T. Murtola, R. Schulz, S. Páll, J. C. Smith, B. Hess, and E. Lindahl, "GROMACS: High performance molecular simulations through multi-level parallelism from laptops to supercomputers," SoftwareX **1–2**, 19 (2015).
[91]W. Humphrey, A. Dalke, and K. Schulten, "VMD: Visual molecular dynamics," J. Mol. Graphics **14**, 33 (1996).
[92]A. Kohlmeyer and J. Vermaas, Akohlmey/Topotools: Release 1.7, 2017.
[93]A. Jain, S. P. Ong, W. Chen, B. Medasani, X. Qu, M. Kocher, M. Brafman, G. Petretto, G. M. Rignanese, G. Hautier, D. Gunter, and K. A. Persson, "FireWorks: A dynamic workflow system designed for high-throughput applications," Concurr. Comput. -Pract. Exper. **27**, 5037 (2015); arxiv:1302.5679v1.
[94]T. S. G. Olsson and M. Hartley, "Lightweight data management with dtool," PeerJ **7**, e6562 (2019).
[95]A. Stukowski, "Visualization and analysis of atomistic simulation data with OVITO–the Open Visualization Tool," Modell. Simul. Mater. Sci. **18**, 015012 (2009).